Supporting Information for "Spatial variability of turbulent mixing from an underwater glider in a large, deep stratified lake"

Oscar Sepúlveda Steiner[1,2], Alexander L. Forrest[3,4], Jasmin B. T. McInerney[3], Bieito Fernández Castro[2,5], Sébastien Lavanchy[2], Alfred Wüest[1,2], and Damien Bouffard[1]

[1]Eawag, Swiss Federal Institute of Aquatic Science and Technology, Surface Waters – Research and Management, Kastanienbaum, Switzerland.

[2]Physics of Aquatic Systems Laboratory, Margaretha Kamprad Chair, Institute of Environmental Engineering, ENAC, École Polytechnique Fédérale de Lausanne, Lausanne, Switzerland.

[3]Civil & Environmental Engineering, University of California – Davis, Davis, CA, USA.

[4]UC Davis Tahoe Environmental Research Center, Incline Village, NV, USA.

[5]Ocean and Earth Sciences, National Oceanography Centre, University of Southampton, Southampton, UK

Contents of this file

This document displays several supplementary materials referenced according to their appearance in the main manuscript. It includes:

1. Text S1
2. Figures S1 to S13
3. Tables S1

Corresponding author: Oscar SÉPULVEDA STEINER (oscar.sepulvedasteiner@eawag.ch)

Text S1.

To address the lack of direct measurements of glider's along-path speeds, we used the dynamic flight model of (Merckelbach et al., 2019). This methodology builds on the steady-state flight model of (Merckelbach et al., 2010), where glider buoyancy, drag and lift forces are balanced out neglecting accelerations. Following this framework, U and angle of attack are calculated using measured pitch angle and changes in buoyancy accounted by the oil bladder volume. The dynamic model considers momentum variations induced by accelerations of the submerged body and flow changes around it. This results in an initial value problem and therefore a numerical solution needs to be implemented (e.g. Runge-Kutta methods). Estimations of parameters such as drag coefficients (parasite and motion-induced), glider volume and lift-angle are obtained by coupling the numerical solution to a cost function which is then minimized.

The implementation was carried out by using the open-source codes provided by Merckelbach (2018). Ambient freshwater density was calculated from CTD data using TEOS 2010 (McDougall & Barker, 2011). The model initialization requires an initial guess of the parameters to be calibrated. We considered parasite and motion-induced drag, $C_{D_o} = 0.15$ and $C_{D_1} = 10.5$, respectively, following Merckelbach et al. (2010, 2019). The mass of glider *Storm Petrel* with the mounted MicroRider was $m_g = 63.6$ kg. With this value, the glider volume was obtained from $V_g = m_g \rho_o^{-1}$, where $\rho_o = 1000$ kg m^{-3} is the freshwater reference density. The lift-angle coefficient was initialized as $a_h = 3.8$ rad^{-1} (Merckelbach et al., 2019). The dynamic flight model was launched for each mission using the first 10'000 values between 10 and 100 m depth, for calibration purposes. Using the calibrated parameters, we obtained full-mission estimates of U and angle of attack for each mission.

Figure S1 shows an example of flight model results. Except for dive/climbs performed during horizontal turns (e.g. change heading from W to N), the data presented corresponds well with the flight behavior for all our missions. Pitch angles were approximately 19° and -21° for dives and climbs, respectively (without considering hovering). This difference is presumably due to differences in battery angle during dives and climbs (Fer et al., 2014). The angle of attack was relatively constant, yet more stable for dives ($3^\circ \pm 0.3^\circ$) than for climbs ($3^\circ \pm 1^\circ$). Along-path speeds for dives (0.3 m s^{-1}) were slower than for climbs (0.4 m s^{-1}). Resulting U values fall within the speed range validated by Merckelbach et al. (2019) using a glider equipped with an electromagnetic current sensor. Flight model results are therefore considered of sufficient quality to be integrated into the turbulence estimation procedure.

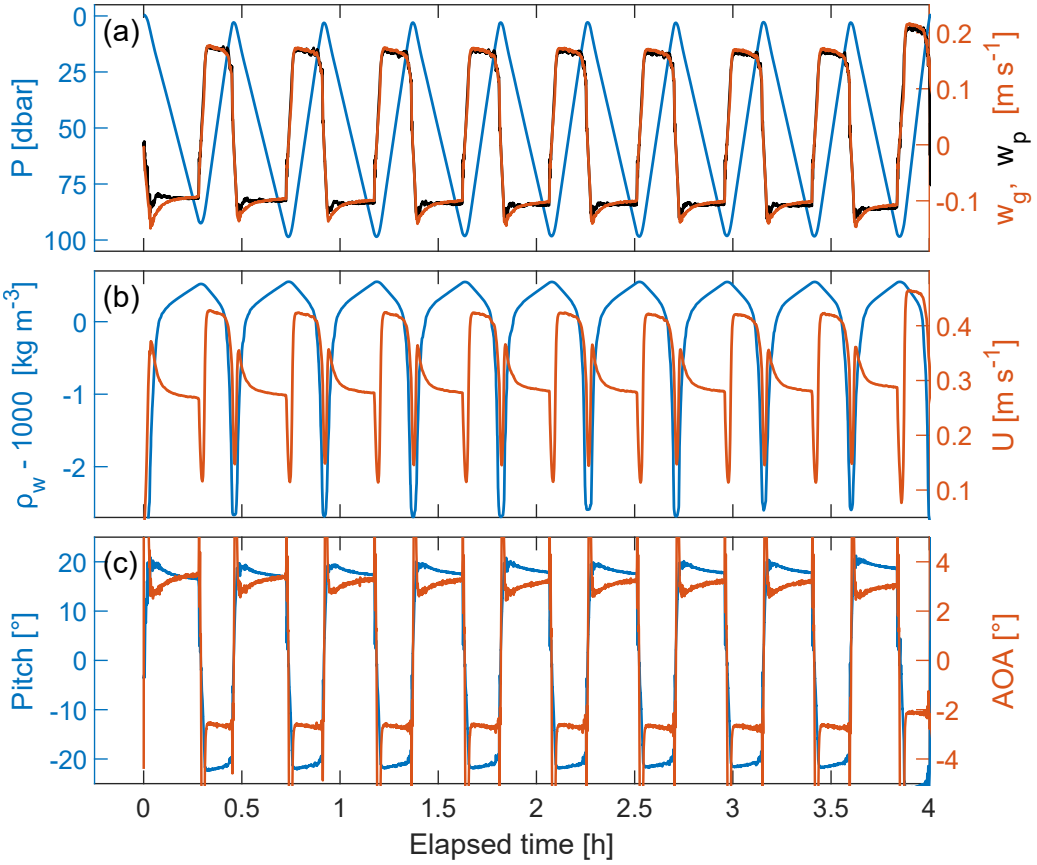

Figure S1. Example of flight model results for mission M1. Time series as elapsed time from the start of M1 on 30 Jul 2018 at ∼10:50 am. Results are presented as in Fer et al. (2014). Model inputs and outputs are depicted by blue and red lines, respectively. (a) Measured pressure (P; blue) accompanied by the glider vertical sinking speed deducted from the flight model (w_g; red). The black line corresponds to the vertical speed w_p inferred from P change. (b) Density (blue) and along path speed (U; red). (c) Pitch angle (blue) and angle of attack (AOA; red). AOA is presented with sign to distinguish dives from climbs.

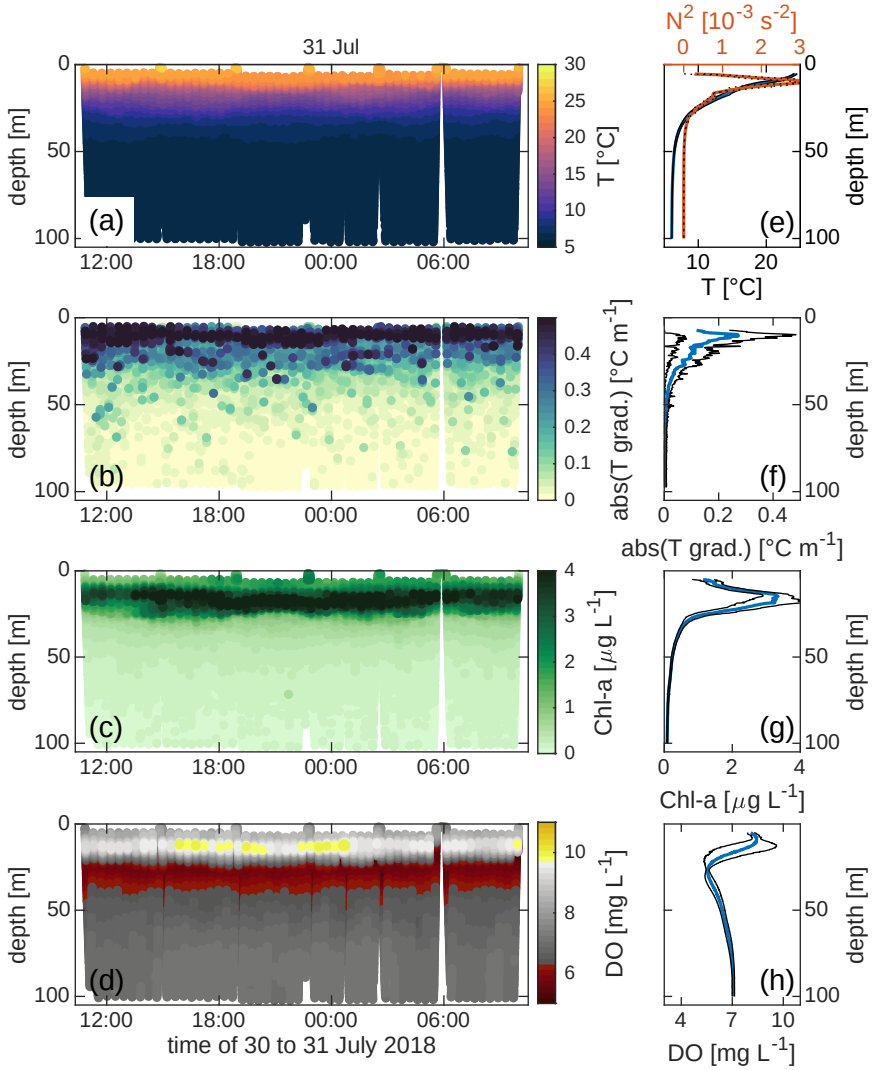

Figure S2. Glider data collected on 30 July 2018 during mission **M1**. (a) Temperature (T). (b) Absolute value of the temperature gradient measured with the MicroRider, sub-sampled at 4 Hz for visualization. (c) Chlorophyll-a (Chl-a). (d) Dissolved oxygen (DO). The tilted DO vertical structure in (d) shows that differences between dives and climbs were unfortunately not adequately corrected. (e-h) Time-averaged profiles (blue lines) of measurements presented in (a-b), accompanied by their respective standard deviations (black line envelopes). Additionally, (e) shows the depth-averaged stability (N^2) profile for this mission (red line) with its standard deviation (black dotted envelope).

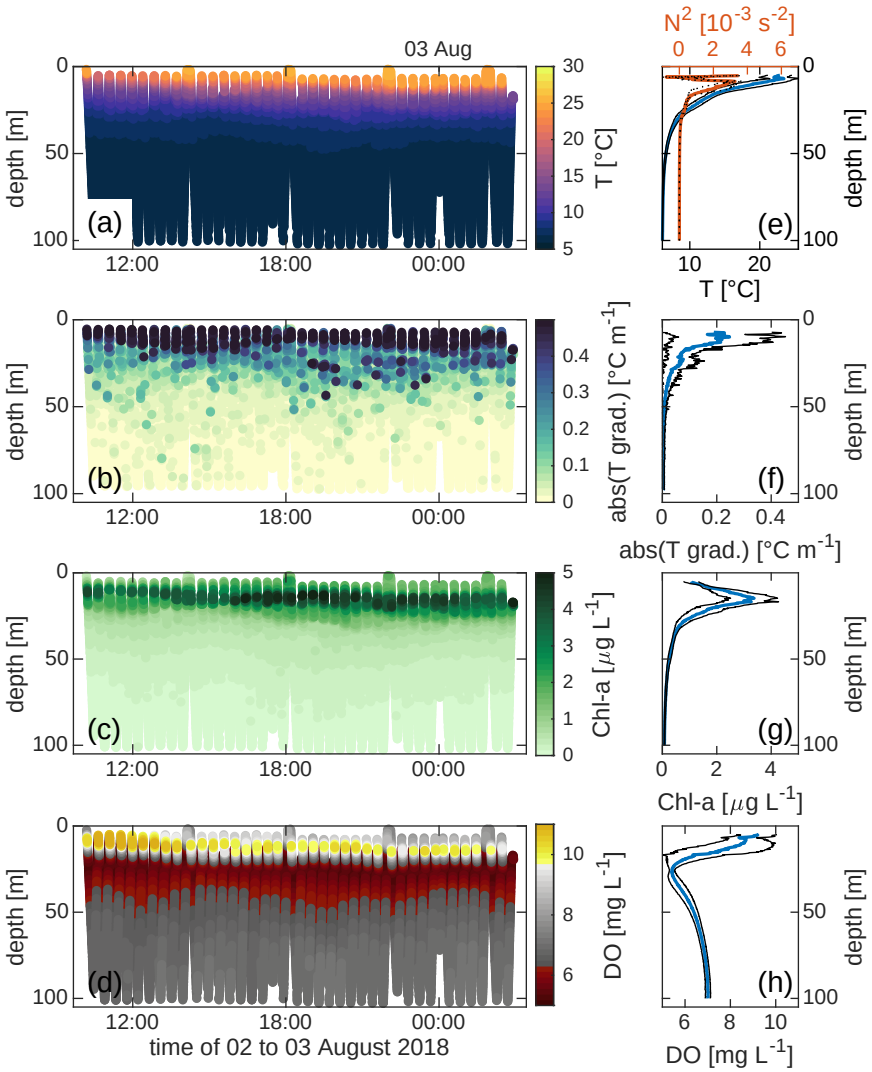

Figure S3. Glider data collected on 2/3 August 2018 during mission **M2**. All panels are analogous to Figure S2.

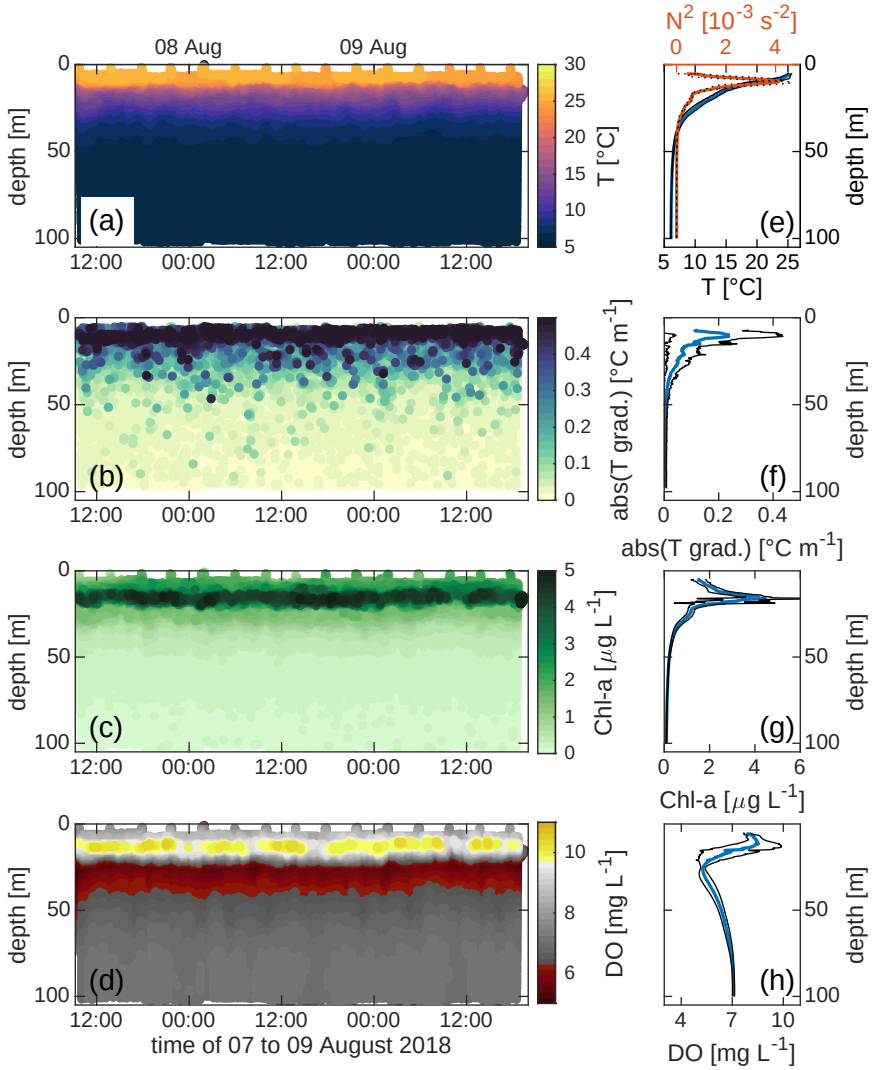

Figure S4. Glider data collected on 7/9 August 2018 during mission **M3**. All panels are analogous to Figure S2.

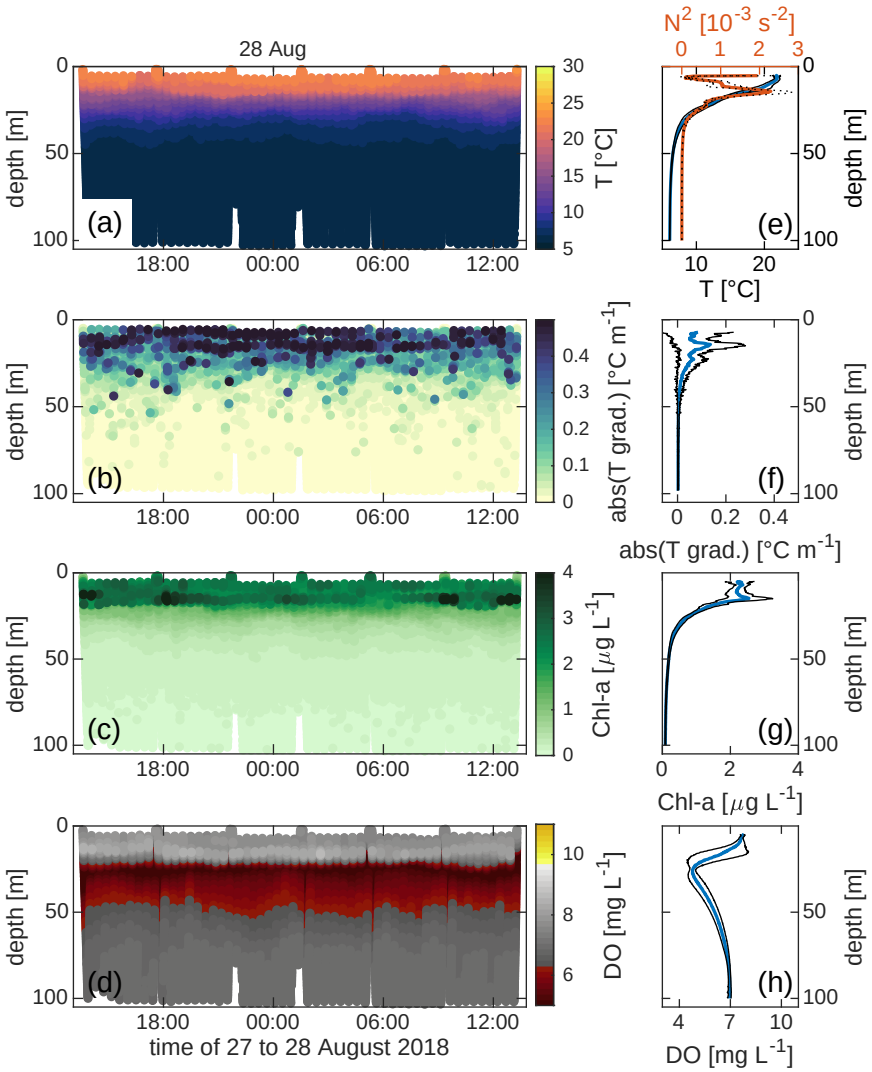

Figure S5. Glider data collected on 27/28 August 2018 during mission **M4**. All panels are analogous to Figure S2.

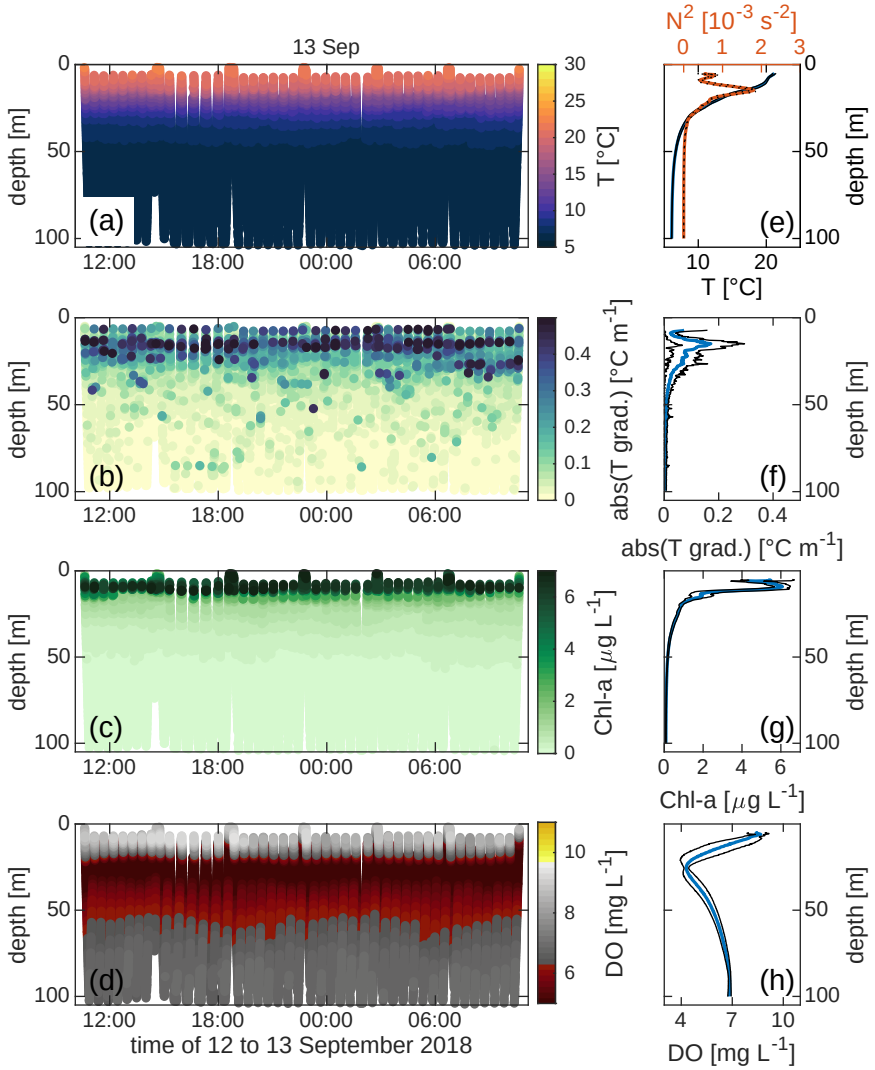

Figure S6. Glider data collected on 12/13 September 2018 during mission **M5**. All panels are analogous to Figure S2.

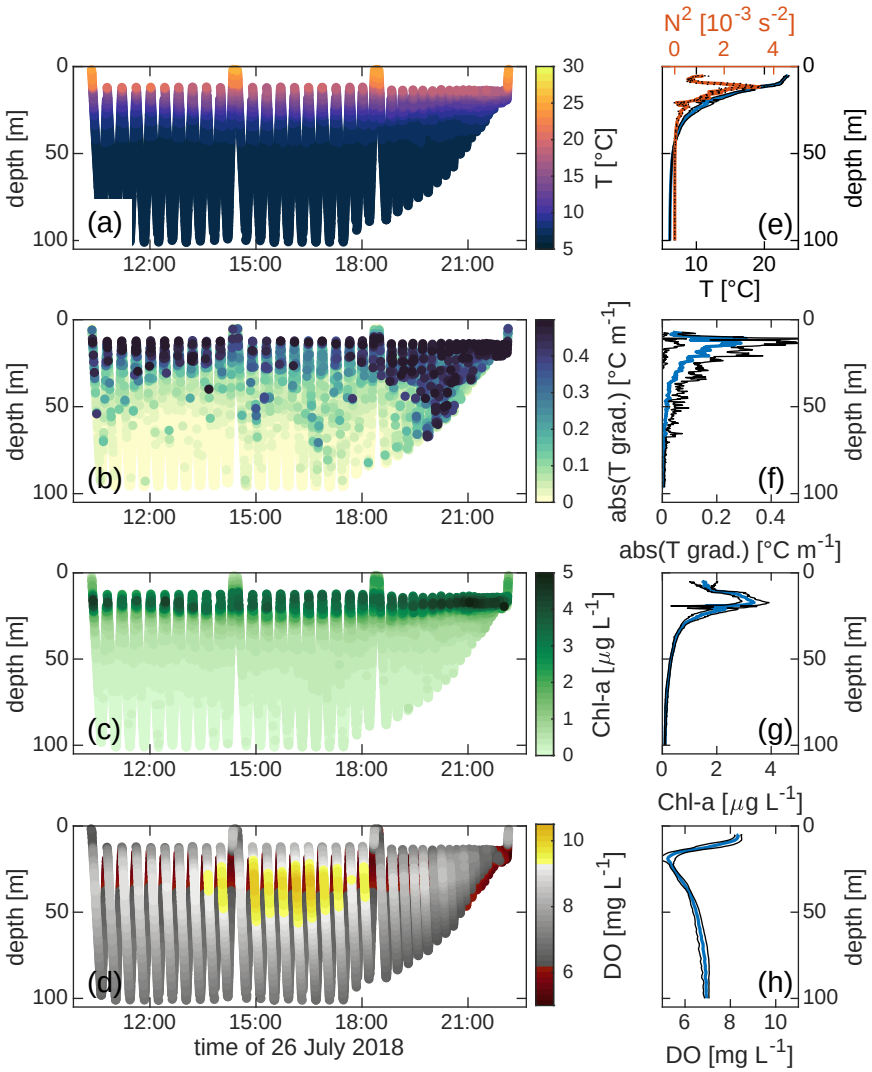

Figure S7. Glider data collected on 26 July 2018 during mission **M0** (interior-to-coast transition). All panels are analogous to Figure S2. For this mission, due to an electronic malfunction of the DO sensor during upward profiles, the DO vertical profile considers downward profiles only.

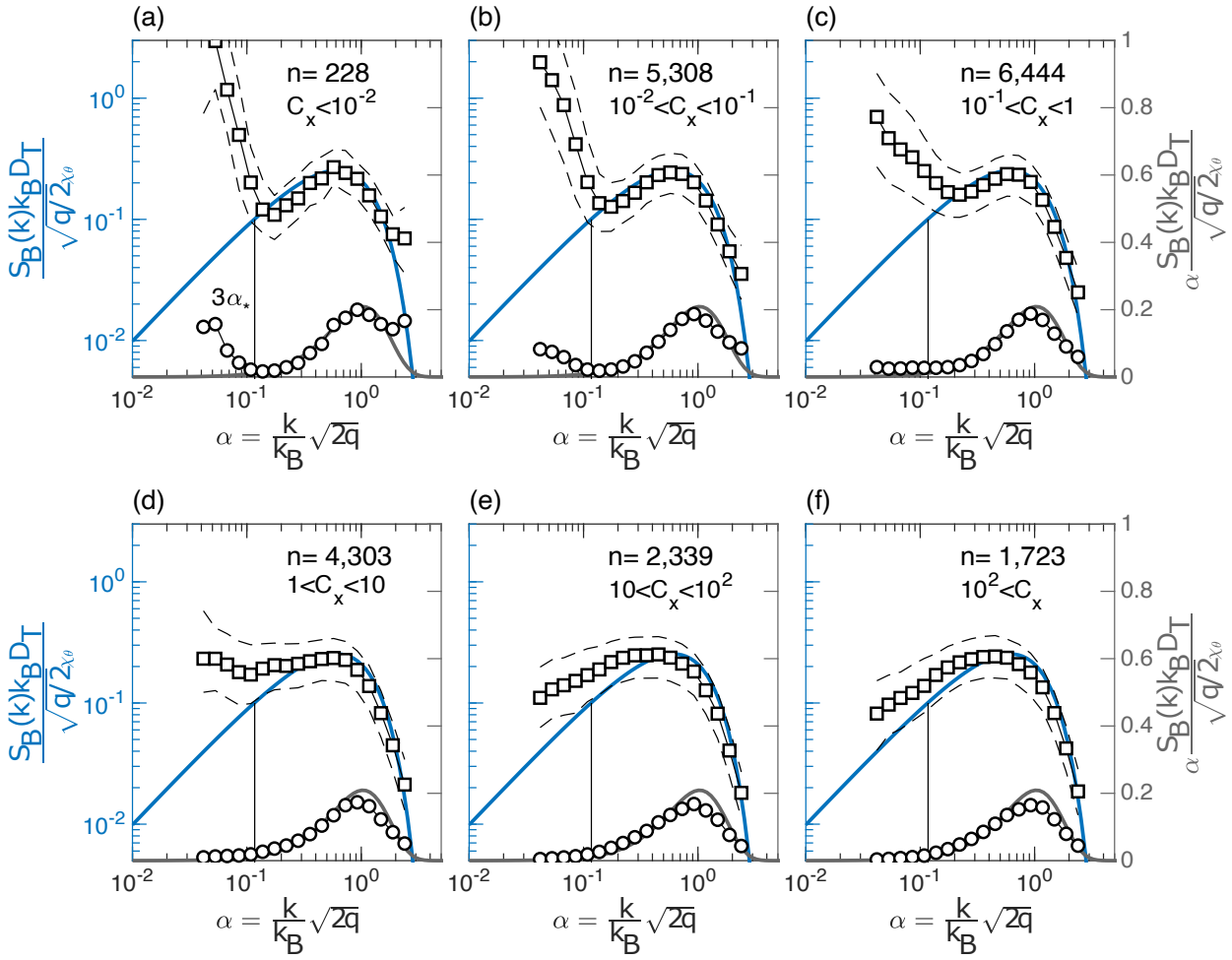

Figure S8. Spectral statistics for **downward** casts, following Dillon and Caldwell (1980). The figure reads analogously to Figure 5 in the main text.

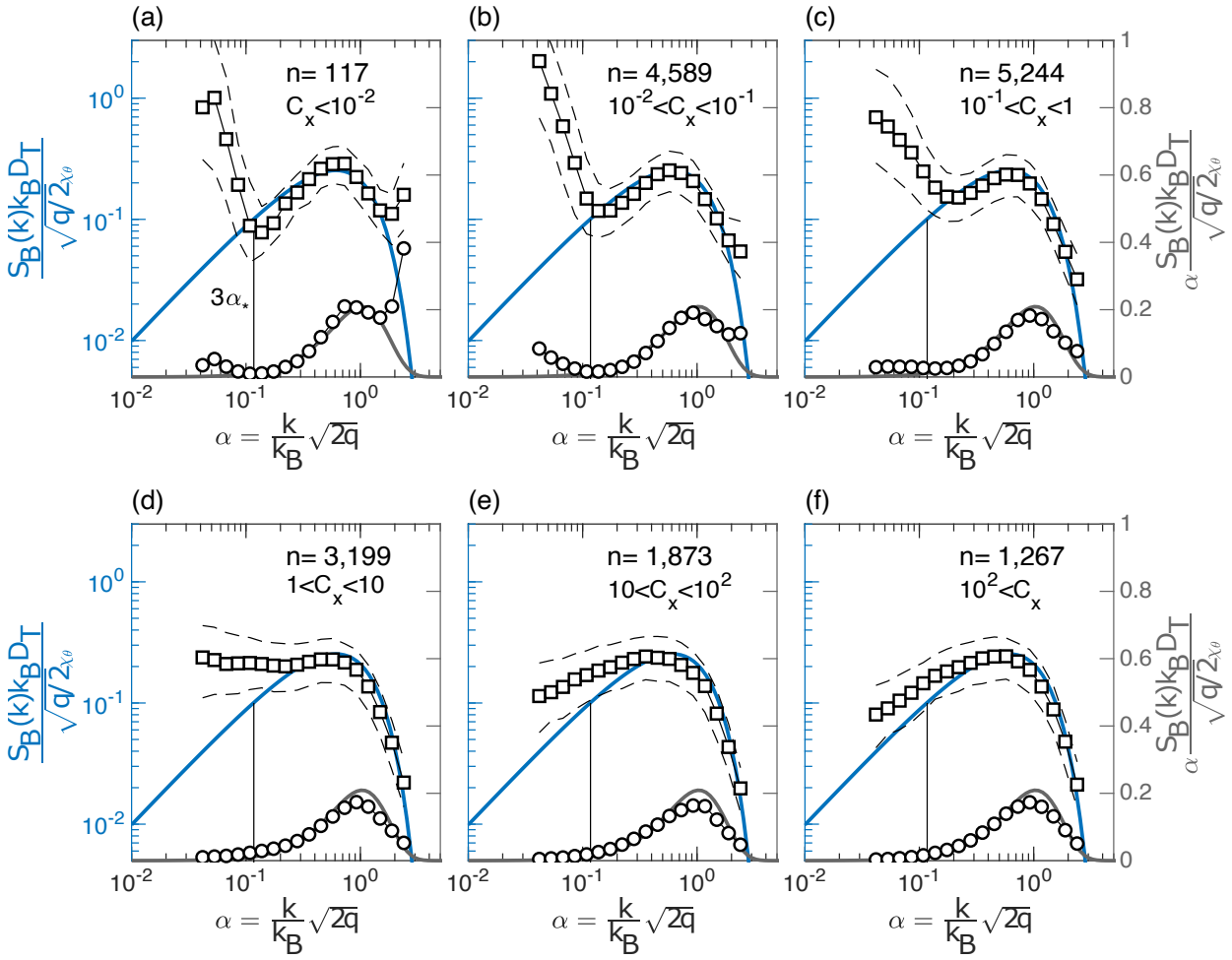

Figure S9. Spectral statistics for **upward** casts, following Dillon and Caldwell (1980). The figure reads analogously to Figure 5 in the main text.

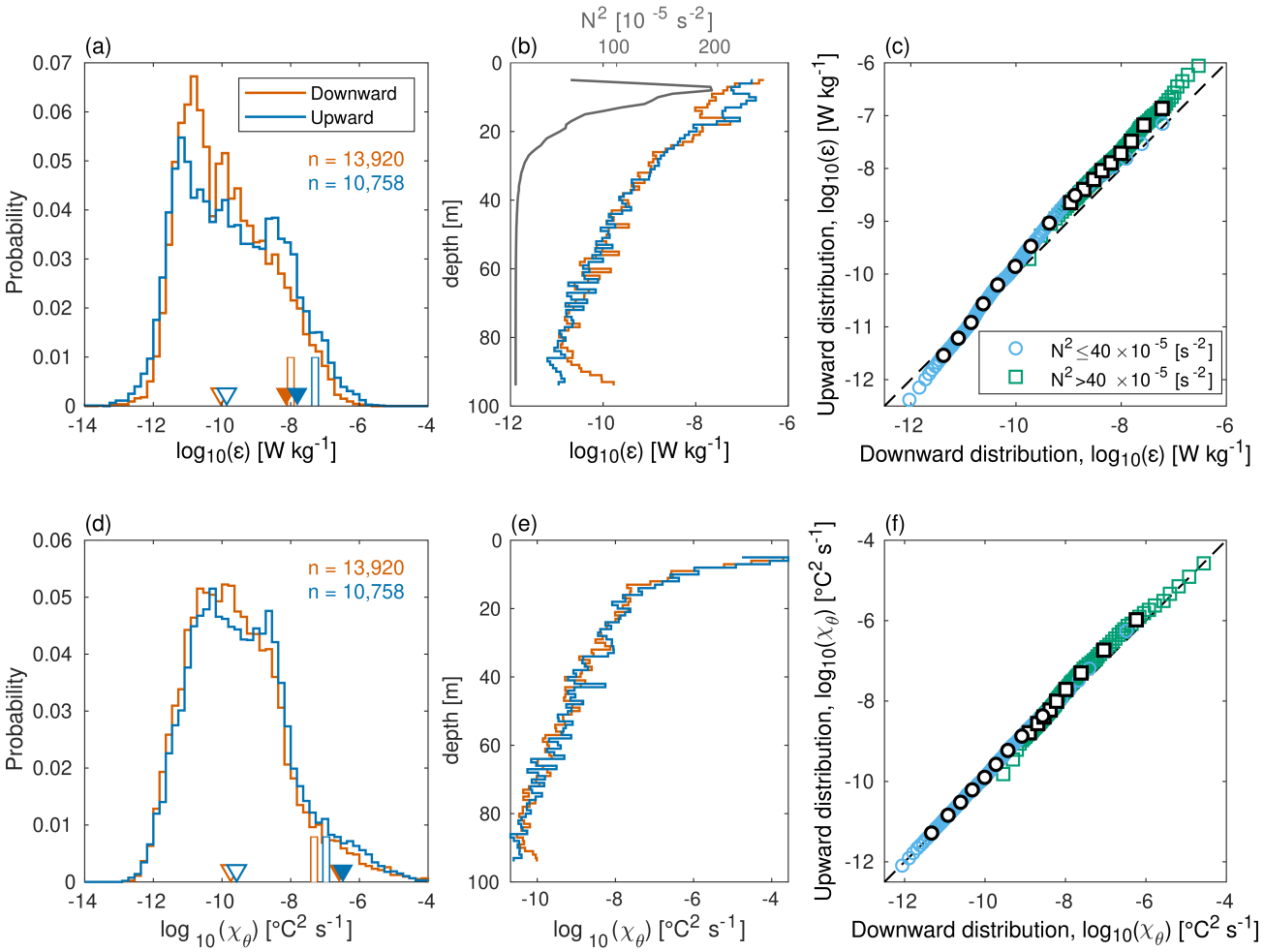

Figure S10. Statistical comparison of upward and downward turbulent dissipation estimates. (a,d) Probability distributions of turbulent dissipation ε and smoothing rate of temperature variance χ_θ, respectively, for the whole data set separated by downward (dives; red) and upward (climbs; blue) casts. Vertical bars correspond to the mle-mean for a log-normal distribution (Baker & Gibson, 1987), while empty and filled triangles represent the median and arithmetic mean, respectively. (b,c) Depth-averaged mle-mean profiles. The gray line in (b) corresponds to the depth-averaged stability (N^2) . (c,f) Q-Q plots comparing downward and upward distributions of turbulent quantities grouped by upper stratified layer ($N^2 > 40 \times 10^{-5}$ s^{-2}) and hypolimnion ($N^2 \leq 40 \times 10^{-5}$ s^{-2}).

Table S1. Statistics of measured turbulent characteristics for different subsets of interest. First row: Statistics of the whole data set ("All") for reference, followed by downward (dives) and upward (climbs) casts. Second row: Statistics of water column subsets as a function of stratification (as defined in the main text). Results are reported twofold: (i) mle-mean for lognormal distribution following Baker and Gibson (1987) accompanied by its intermittency factor $\langle\sigma^2_{mle}\rangle$, (ii) median values with its respective 25th and 75th quantiles.

Parameter	Estimator	All	Downward	Upward
ε [10^{-8} W kg^{-1}]	mle-mean $\langle\sigma^2_{mle}\rangle$	2.1 $\langle$9.7$\rangle$	1.0 $\langle$8.6$\rangle$	5.1 $\langle$11.2$\rangle$
	median [25^{th}, 75^{th}]	0.011 [0.0013, 0.17]	0.0095 [0.0013, 0.12]	0.014 [0.0011, 0.28]
χ_θ [10^{-8} °C^2 s^{-1}]	mle-mean $\langle\sigma^2_{mle}\rangle$	7.2 $\langle$10.9$\rangle$	5.0 $\langle$10.5$\rangle$	11.1 $\langle$11.4$\rangle$
	median [25^{th}, 75^{th}]	0.021 [0.0026, 0.23]	0.019 [0.0023, 0.19]	0.027 [0.0029, 0.29]
		Epilimnion	Metalimnion	Hypolimnion
ε [10^{-8} W kg^{-1}]	mle-mean $\langle\sigma^2_{mle}\rangle$	27.0 $\langle$7.0$\rangle$	9.2 $\langle$2.6$\rangle$	0.60 $\langle$8.1$\rangle$
	median [25^{th}, 75^{th}]	1.3 [0.21, 5.0]	2.6 [0.81, 7.6]	0.0076 [0.0011, 0.086]
χ_θ [10^{-8} °C^2 s^{-1}]	mle-mean $\langle\sigma^2_{mle}\rangle$	846.5 $\langle$11.6$\rangle$	400.4 $\langle$7.4$\rangle$	1.2 $\langle$8.3$\rangle$
	median [25^{th}, 75^{th}]	2.2 [0.19, 40.3]	8.1 [1.3, 62.9]	0.015 [0.0022, 0.14]

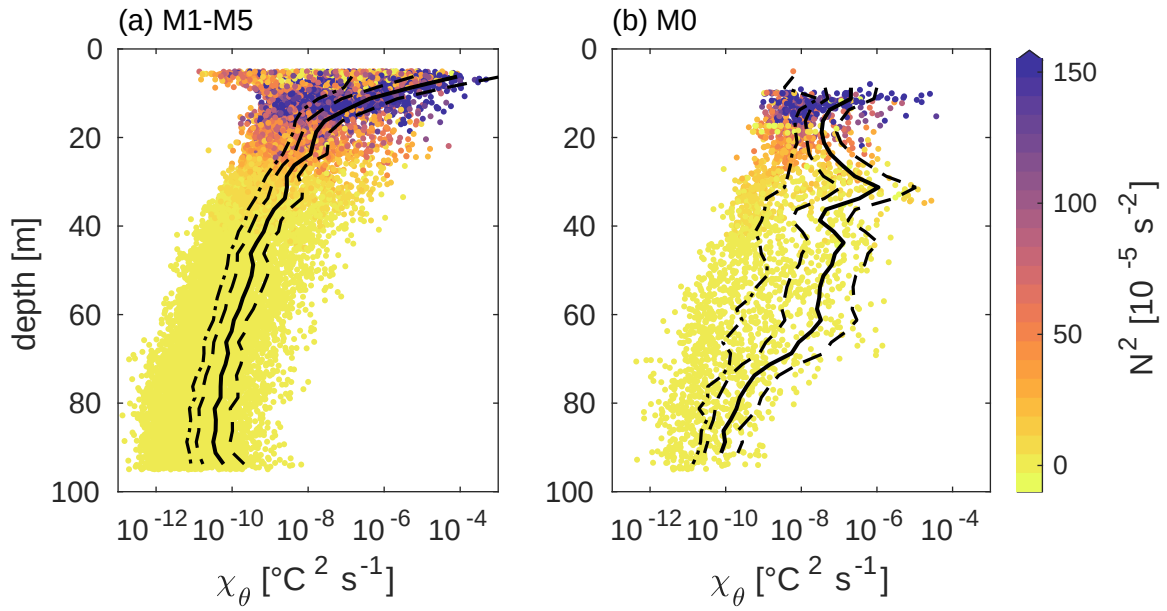

Figure S11. Vertical distribution of measured smoothing rate of temperature variance (χ_θ). (a) Interior (M1-M0) and (b) coastal (M0). Thick black line and dashed envelope correspond to the mle-mean and statistical variability given by the intermittency factor, respectively. The dot-dashed line represents the median. Data selection criteria is the same as in Figures 6 and 7 (main text).

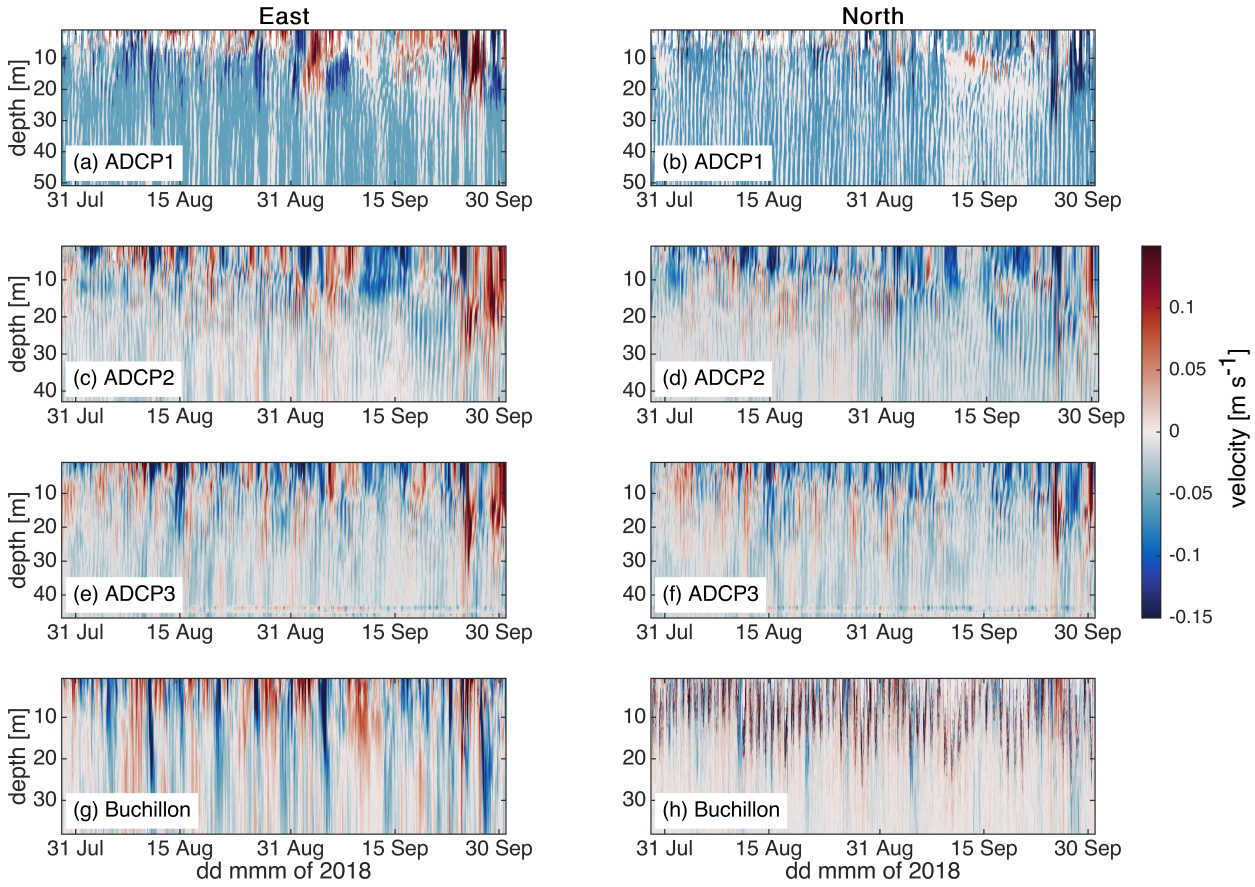

Figure S12. Time series of ADCP measurements. The location of each station is indicated in Figure 2 (main text).

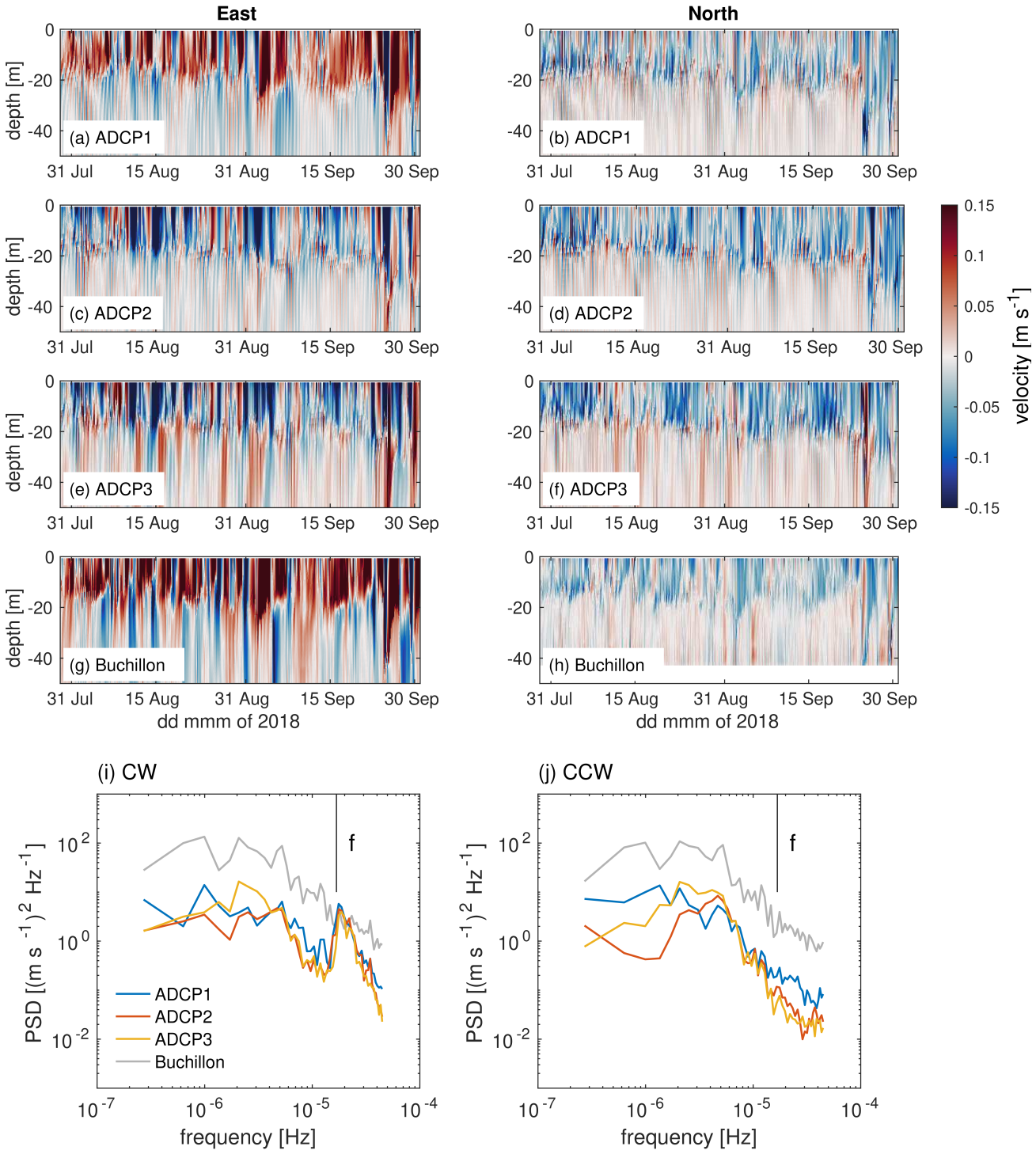

Figure S13. Meteolakes currents data (a-h) at the different stations examined in-situ and respective median rotary spectra analysis (i,j) showing the same energy peak in the inertial frequency band in the clockwise (CW; anti-cyclonic in the north hemisphere) spectra as the ADCP measurements presented in Figure 10 (main text). CCW stands for counter-clockwise (i.e., cyclonic).

References

Baker, M. A., & Gibson, C. H. (1987). Sampling turbulence in the stratified ocean: Statistical consequences of strong intermittency. *Journal of Physical Oceanography*, *17*(10), 1817–1836. doi: https://doi.org/10.1175/1520-0485(1987)017⟨1817:STITSO⟩2.0.CO;2

Dillon, T. M., & Caldwell, D. R. (1980). The Batchelor spectrum and dissipation in the upper ocean. *Journal of Geophysical Research*, *85*(C4), 1910–1916. doi: https://doi.org/10.1029/JC085iC04p01910

Fer, I., Peterson, A. K., & Ullgren, J. E. (2014). Microstructure measurements from an underwater glider in the turbulent Faroe Bank Channel overflow. *Journal of Atmospheric and Oceanic Technology*, *31*(5), 1128–1150. doi: https://doi.org/10.1175/JTECH-D-13-00221.1

McDougall, T. J., & Barker, P. (2011). Getting started with TEOS-10 and the Gibbs Seawater (GSW) oceanographic toolbox. *SCOR/IAPSO WG.*, *127*, 1–28.

Merckelbach, L. (2018). Initial release of Glider flight model. Version 1.0.1. *Zenodo*. doi: https://doi.org/10.5281/zenodo.2222694

Merckelbach, L., Berger, A., Krahmann, G., Dengler, M., & Carpenter, J. R. (2019). A dynamic flight model for Slocum gliders and implications for turbulence microstructure measurements. *Journal of Atmospheric and Oceanic Technology*, *36*(2), 281–296. doi: https://doi.org/10.1175/JTECH-D-18-0168.1

Merckelbach, L., Smeed, D., & Griffiths, G. (2010). Vertical water velocities from underwater gliders. *Journal of Atmospheric and Oceanic Technology*, *27*(3), 547–563. doi: https://doi.org/10.1175/2009JTECHO710.1